Trochoidal X-ray Vector Radiography: Directional dark-field without grating stepping

Y. Sharma, S. Bachche, M. Kageyama, M. Kuribayashi, F. Pfeiffer, T. Lasser, and A. Momose

View Online   Export Citation   CrossMark

ARTICLES YOU MAY BE INTERESTED IN

Dual phase grating interferometer for tunable dark-field sensitivity
Applied Physics Letters **110**, 014105 (2017); https://doi.org/10.1063/1.4973520

Large field-of-view tiled grating structures for X-ray phase-contrast imaging
Review of Scientific Instruments **88**, 015104 (2017); https://doi.org/10.1063/1.4973632

Implementation of a double-grating interferometer for phase-contrast computed
tomography in a conventional system nanotom$^{®}$ m
APL Bioengineering **2**, 016106 (2018); https://doi.org/10.1063/1.5022184

Trochoidal X-ray Vector Radiography: Directional dark-field without grating stepping

Y. Sharma,[1,2,3] S. Bachche,[3] M. Kageyama,[4] M. Kuribayashi,[4] F. Pfeiffer,[1,5] T. Lasser,[2] and A. Momose[3]

[1]*Chair of Biomedical Physics, Department of Physics and School of BioEngineering, Technical University of Munich, 85748 Garching, Germany*
[2]*Computer Aided Medical Procedures, Department of Informatics, Technical University of Munich, 85748 Garching, Germany*
[3]*Institute of Multidisciplinary Research for Advanced Materials (IMRAM), Tohoku University, Sendai, Miyagi 980-8577, Japan*
[4]*Rigaku Corporation, Tokyo 196-8666, Japan*
[5]*Department of Diagnostic and Interventional Radiology, Klinikum rechts der Isar, Technical University of Munich, 81675 München, Germany*

X-ray Vector Radiography (XVR) is an imaging technique that reveals the orientations of sub-pixel sized structures within a sample. Several dark-field radiographs are acquired by rotating the sample around the beam propagation direction and stepping one of the gratings to several positions for every pose of the sample in an X-ray grating interferometry setup. In this letter, we present a method of performing XVR of a continuously moving sample without the need of any grating motion. We reconstruct the orientations within a sample by analyzing the change in the background moire fringes caused by the sample moving and simultaneously rotating in plane (trochoidal trajectory) across the detector field-of-view. Avoiding the motion of gratings provides significant advantages in terms of stability and repeatability, while the continuous motion of the sample makes this kind of system adaptable for industrial applications such as the scanning of samples on a conveyor belt. Being the first step in the direction of utilizing advanced sample trajectories to replace grating motion, this work also lays the foundations for a full three dimensional reconstruction of scattering function without grating motion. © *2018 Author(s). All article content, except where otherwise noted, is licensed under a Creative Commons Attribution (CC BY) license (http://creativecommons.org/licenses/by/4.0/).* https://doi.org/10.1063/1.5020361

Attenuation based X-ray imaging has been in use for more than a hundred years, and there have been significant advancements in increasing the spatial resolution over the years.[1] Nowadays, we have commercial devices that provide resolution at the micro- and nano-meter scales. However, these systems suffer from a trade-off between the spatial resolution and the size of the sample that can be measured.[2] Dark-field imaging is a relatively new X-ray contrast mechanism which provides information about small and ultra-small angle scattering of X-rays with the spatial resolution of an imaging system.[3] This means that it is possible to probe micron and sub-micron sized structures within centimeter sized samples, resulting in a significant advantage over point-wise scanning methods.[7] The theoretical foundations of this contrast mechanism have been established recently.[4–6] In particular, it has been shown that the dark-field signal encodes the real space autocorrelation function of a system with the highest sensitivity to a certain specific correlation length, depending on the geometry of the measurement. Though newly developed, X-ray dark-field imaging has shown promising results in several fields including lung imaging,[8] mammography,[9] cardiac imaging,[10] and non-destructive testing.[11,12]

Dark-field contrast is one of the three contrast modes obtained in an X-ray grating interferometry (XGI) setup, the other two being differential phase contrast and the conventional attenuation contrast. A typical XGI setup consists of three diffraction gratings placed in between the X-ray source and the detector. One of the gratings is stepped to several positions, in a direction orthogonal to the direction of grating bars and in the plane of the gratings, and the intensity in every pixel for every grating position is recorded. By modeling the intensity fluctuation as a sinusoid, we define the attenuation contrast as the decrement in the mean intensity, the differential phase contrast as the shift in the position of the peak, and the dark-field contrast as the decrement in the sinusoidal amplitude which is also known as the loss of visibility. This process is known as the phase stepping method.[13]

The phase stepping method described above suffers from poor temporal resolution and instabilities due to the requirement of very precise grating stepping. While Miao *et al.*[14] replaced grating stepping with electromagnetic stepping of X-ray focal spots as a significant step towards industrially compatible acquisition methods, Kottler *et al.*[15] introduced a stepping free approach known as phase scanning. In the latter approach, the intensity modulation in every pixel is recorded by moving the sample linearly through the detector field-of-view (FOV) that encodes spatially varying phase information in the form of intensity, known as moire fringes. Several works[16,17] using this approach have been reported in recent years. All of them require a very precise and uniform arrangement of moire fringes in the FOV or, in other words assume a well-defined and homogeneous grating

structure. However, owing to the imperfections in the fabrication process, it is almost impossible to guarantee the homogeneity of the grating structure. To overcome this limitation, Bachche *et al.*[18] recently proposed a robust phase scanning method that works with irregular and varying moire patterns.

Irrespective of the method employed (phase stepping or phase scanning), a single dark-field image is not sufficient to obtain the complete scattering information. Owing to its anisotropic nature[19] arising from the uni-directional specificity of a grating interferometry setup using linear gratings, the dark-field signal varies with the orientation of the sample with respect to the grating bars. Hence, to measure the dark-field signal completely, we need to obtain several dark-field images at different poses of the sample. This has been accomplished by using a technique known as X-ray Vector Radiography (XVR).[20–24] XVR is a technique that calculates the two-dimensional orientation of the micro-structure within a sample by using several dark-field images obtained by a phase stepping procedure at different angular poses of the sample (typically placed on an Euler cradle) around the beam propagation direction. It has been shown useful for analyzing the micro-structure of composite materials[21,24] and biological specimen.[20,22,23]

The XVR method discussed above requires a time-consuming stepwise process involving rotation of the sample to several poses and a phase-stepping procedure for every pose. Translation of gratings with period in the range of a few micrometers induces additional chances of vibration and instabilities leading to erroneous results in a conventional XGI setup. A single shot method for XVR was recently proposed by Kagias *et al.*[25] with a specialized phase grating; however, it requires a high resolution detector and a brilliant X-ray source. To overcome these limitations, we present a method that does not require any grating translation during the measurement, works with laboratory X-ray sources, and is suitable for fast scanning of continuously moving samples placed on a commonly used industrial stage. Below, we present details of our method.

We use a vertical setup, which was reported in Ref. 18, with an X-ray source propagating X-rays vertically from bottom to the top of the setup. The X-ray source (UltraX 18, Rigaku, Japan) comprising a tungsten rotating anode is operated at a tube voltage of 40 kV and a tube current of 70 mA. Three gratings are arranged along the length of the setup in the first order Talbot configuration as shown in Fig. 1. A photon counting detector (Hypix-3000, Rigaku, Japan) is used with the lower threshold set to 15 keV. The above settings have been optimized for maximizing the product of visibility and square root of intensity for the setup. A rotation stage with a hole on its axis of rotation, which coincides with the beam propagation direction (z axis in Fig. 1), is mounted on a linear stage allowing motion in the x direction. The combination of the rotational and linear stages allows a trochoidal motion of the sample in a two-dimensional plane orthogonal to the beam propagation direction.

Prior to the measurement, we need to establish a field of moiré pattern in the detector FOV. This is done by rotationally misaligning the gratings G1 and G2 slightly, resulting in moiré fringes as seen in Fig. 2. We can see in Fig. 2 that the fringes are not uniform due to slight inhomogeneities in the
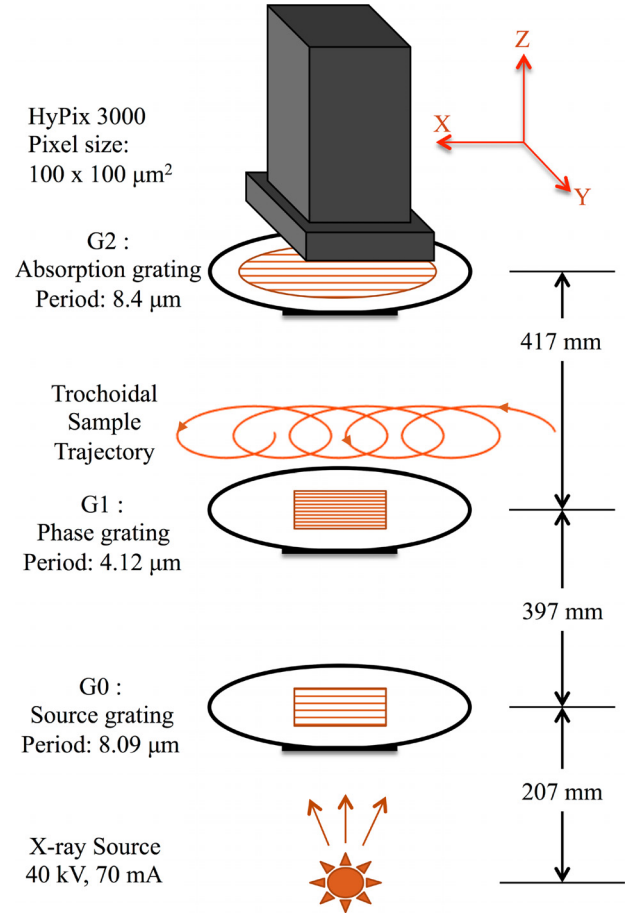

FIG. 1. Schematic of a vertical grating interferometer setup used for Trochoidal X-ray Vector Radiography (TXVR).

grating structure. Next, we perform a standard phase stepping procedure by displacing G2 in steps over one period and calculate the background absorption $A_0(x, y)$, differential phase $\phi_0(x, y)$, and visibility $V_0(x, y)$ images, where (x, y) denotes the coordinates of pixels in the detector plane. Sometimes, it is required to tune the grating alignment in order to ensure that the values of ϕ_0 span the range $[-\pi, \pi]$ along the x direction for every row y in the FOV. Once this is achieved, we discretize the 2D moire field into n regions represented by indicator matrices F_k

$$F_k(x,y) = \begin{cases} 1, \text{ if } -\pi + \dfrac{2\pi(k-1)}{n} < \phi_0(x,y) \leq -\pi + \dfrac{2\pi k}{n}, \\ 0, \text{ otherwise} \end{cases}$$
$$k = 1, 2, \ldots, n. \qquad (1)$$

The number of pixels in every row y in each indicator matrix is stored in the vector $N_k(y)$.

Let us consider a point on the sample which is located at a distance r from the centre of rotation and makes a counterclockwise angle α with the positive x axis at time $t = 0$, such that its cartesian coordinates in the sample frame can be written as

$$p = r\cos(\alpha), \quad q = r\sin(\alpha). \qquad (2)$$

The motion of this point on the detector plane, with (x, y) denoting the coordinates of a detector pixel, can be written as
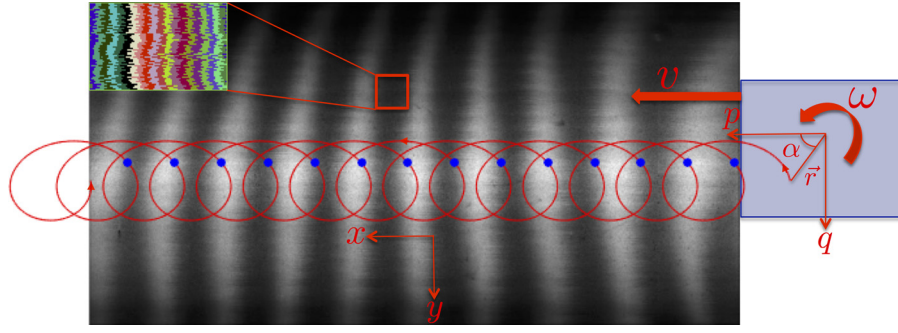
FIG. 2. Detector FOV with 775×385 pixels (top view from Fig. 1). We can see moire fringes introduced by slightly rotating the gratings G1 and G2 with respect to each other. The phase image without the sample is discretized into n bins as shown in the zoomed inset [Eq. (1)], which is used for the algorithm of image formation [Eq. (8)]. The trajectory of a point (p, q) on the sample [Eq. (3)] is shown in red. Blue points show the position of this point at times T_θ corresponding to the same sample pose θ [Eq. (7)].

$$x = rM \cos(\omega t + \alpha) + ut, \quad y = rM \sin(\omega t + \alpha), \quad (3)$$

where ω is the angular speed of the sample rotation, M is the magnification of the system, and u is the linear speed of the sample on the detector plane with unit of pixels/s. u is related to the speed of the linear stage v by

$$u = \frac{v \cdot M}{d}, \quad (4)$$

where d is the detector pixel size. Let

$$H(p, q, t) = \left[H_x(p, q, t), H_y(p, q, t) \right], \quad (5)$$

where $H_x(p, q, t)$ and $H_y(p, q, t)$ are functions that relate the detector coordinates x and y, respectively, to the sample coordinates (p, q) at time t. $H_x(p, q, t)$ and $H_y(p, q, t)$ can be easily derived from Eqs. (2) and (3). The motion described by Eq. (3) falls under one of the three special cases of a trochoid, namely, cycloid, curtate cycloid, or prolate cycloid, depending on the ratio of the linear speed and the tangential speed at the distance r from the centre of rotation. Therefore, we use trochoid as the generic term to describe the motion of the sample and term our method as Trochoidal X-ray Vector Radiography (TXVR).

We acquire movie frames $I_t(x, y)$ at time $t \in T$, where

$$T = \left\{ 0, \frac{1}{f}, \frac{2}{f}, \dots, \frac{N_F}{f} \right\}, \quad (6)$$

with f being the detector frame rate and N_F the total number of frames recorded as the sample moves in a trochoidal trajectory [given by Eq. (3)] across the FOV. Next, we decouple the rotational and linear part of the trochoidal motion by selecting frames $I_t(x, y)$, $t \in T_\theta$, where T_θ is given by

$$T_\theta = \left\{ t \in T : t = \frac{\theta + 2\pi j}{\omega} \text{ for } j \in \mathbb{N} \right\}. \quad (7)$$

The set of frames, acquired at the positions denoted by blue points on the trochoidal trajectory shown in Fig. 2, represents a linear motion of the point (p, q) at a pose θ with respect to the pose at $t = 0$. From this linear movie, we calculate $J_k(\theta, p, q)$ utilizing the algorithm described in Ref. 18

$$J_k(\theta, p, q) = \sum_{t \in T_\theta} \frac{I_t[H(p, q, t)] \cdot F_k[H(p, q, t)]}{A_0[H(p, q, t)] \cdot N_k[H_y(p, q, t)]}. \quad (8)$$

$J_k(\theta, p, q)$ is the stepping curve for every angular position θ of the sample such as the one that would be obtained by the conventional phase stepping approach. It encodes the information about the change in the background phase map caused by the point (p, q) in the sample as it crosses the FOV in the orientation θ. Next, we fit a sinusoid to the stepping curve for every θ

$$J_k(\theta, p, q) \approx a_0(\theta, p, q) + a_1(\theta, p, q) \cos\left[\frac{2\pi}{n} k - \phi(\theta, p, q) \right]. \quad (9)$$

We perform the trochoidal phase scanning procedure described above with the sample in the FOV to obtain the parameters $a_0^s(\theta, p, q), a_1^s(\theta, p, q)$, and $\phi^s(\theta, p, q)$ for the sample and without the sample to obtain $a_0^b(\theta, p, q), a_1^b(\theta, p, q)$, and $\phi^b(\theta, p, q)$ for the background. We can, thus, calculate the absorption and dark-field (visibility) image as

$$A(\theta, p, q) = \frac{a_0^s(\theta, p, q)}{a_0^b(\theta, p, q)},$$

$$V(\theta, p, q) = \frac{a_1^s(\theta, p, q) \cdot a_0^b(\theta, p, q)}{a_1^b(\theta, p, q) \cdot a_0^s(\theta, p, q)}. \quad (10)$$

So far, we obtained the dark-field values $V(\theta, p, q)$ for every pixel (p, q) in the sample. Next, we use these images to calculate the main structure orientation in every pixel. $V(\theta, p, q)$ encodes the variation in the dark-field signal as the orientation θ of the scattering structure with respect to the grating bars is varied over $[0, 2\pi]$. We model this variation as a sinusoid as proposed by Schaff *et al.*[22]

$$-\ln[V(\theta, p, q)] \approx b_0(p, q) + b_1(p, q) \cos\{2[\theta - \gamma(p, q)]\}. \quad (11)$$

Here, $b_0(p, q)$ denotes the mean visibility over all poses, $b_1(p, q)/b_0(p, q)$ is a measure of the degree of anisotropy, and $\gamma(p, q)$ represents the main orientation of the scattering structure in the pixel (p, q).

We show two results of our technique in Fig. 3. The first sample consists of a known arrangement of scattering structures for the proof-of-principle of our technique. It is a rubber pipe reinforced with a crossed arrangement of nylon fibres. We can see in Fig. 3(a) that the orientation of the nylon fibres can be determined using TXVR. The second sample is a small specimen cut out of polypropylene reinforced with glass fibres. The dark part in the middle in Fig. 3(b) is a thick screw hole (female screw) extending out of the plane with a thin
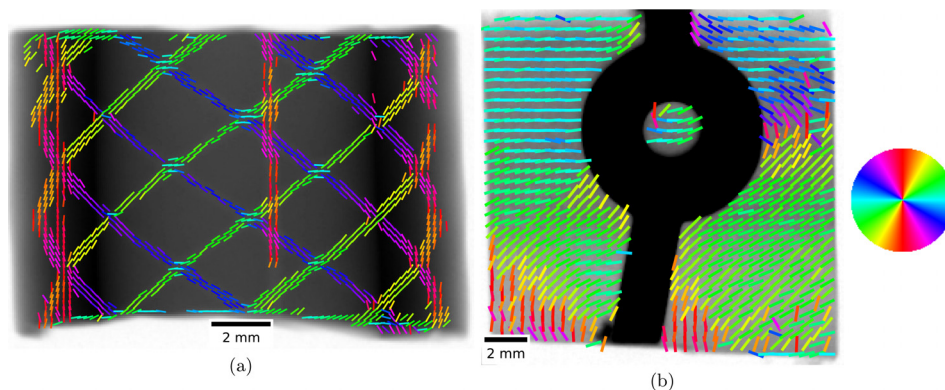
FIG. 3. Examples of results obtained using TXVR. Two dimensional orientations $\gamma(p, q)$ [Eq. (11)] are displayed as color coded unit vectors overlaid on the corresponding gray-scale attenuation image. Coloring is obtained by converting the value of $\gamma(p, q)$ to HSV (Hue, Saturation, and Value) by setting hue equal to $\gamma(p, q)$ and saturation and value equal to 1 for all pixels; the colorwheel on the right should be used for interpreting the colors. (a) Orientations of nylon fibres embedded in a rubber pipe (half cut) calculated using TXVR. The grayscale for the attenuation image is set to [0.29, 1] and the orientation is shown in every third pixel. (b) The orientations of glass fibres overlaid on the attenuation image (grayscale values between [0.6, 1]) for glass fibre reinforced polypropylene. The central part is a thick screw hole, and hence, we mask it out for displaying the orientations of the glass fibres (every seventh pixel) in the thin plate at the bottom of the screw hole.

plate at the bottom. Since the screw hole is too thick for the X-ray energy used, we mask it out and show the TXVR result only for the bottom plate. The colored bars represent the orientations of the glass fibres resulting from the molding process that is used for manufacturing. The orientations of the glass fibres with diameters in the range of a few microns can be determined in this image, which has a pixel size of approximately 70 μm.

For the results shown, we used $\omega = \pi/6$ rad/s, which is the maximum rotation speed of the rotation stage that we used. In order to have sufficient statistics for the stepping curve obtained for every angular position according to Eq. (8), we set the linear speed such that the sample completes 100 full rotations as it crosses the field-of-view. The total scanning distance for the samples used was 80 mm, resulting in a linear speed of $v = 0.0752$ mm/s. The movie is recorded at $f = 1/0.015$ frames/s, resulting in a total of 80 000 frames. Note that no additional blurring is induced as long as the variation of tangential velocity at the farthest point from the center of rotation is less than 1 pixel/frame. This condition is satisfied when the distance of the farthest point from the center of rotation is less than $r_{max} = (d \cdot f)/(\omega \cdot M)$. This condition is satisfied for the size of the sample and the settings used in this work.

The total scan time for the above settings is 20 mins; however, the results shown in Fig. 3 have been obtained by processing only 3100 frames out of the total frames recorded corresponding to 31 unique values of θ resulting in an effective total exposure time of 46.5 s. Using faster rotation and linear speed can significantly reduce the total measurement time. However, for faster rotation, it might be useful to increase the camera frame rate.

To conclude, we have presented a method of measuring the complete dark-field information in an industrially compatible manner. The presented method allows us to indirectly recover quantitative information (orientation) about unresolvable structures, even though the information obtained in a single dark-field image is, so far, non-quantitative. An advanced processing algorithm can be developed to incorporate intensity and visibility modulations in a single model

along with position dependent velocity variation, leading to a further increase in the measurement speed.

TXVR is a two dimensional method, meaning that we measure structure orientations averaged over the thickness of the sample and projected onto a 2D plane. However, the principle of advanced sample trajectories, such as the trochoid used here, can be extended for reconstructing the scattering signal in every three dimensional volume element[26,27] without any grating motion during the acquisition.

See supplementary material for XVR (with phase stepping) results for the sample shown in Fig. 3(b). It can be seen that qualitatively similar results are obtained using XVR and TXVR.

[1]P. J. Withers, Mater. Today **10**, 26 (2007).

[2]V. Cnudde and M. N. Boone, Earth-Sci. Rev. **123**, 1 (2013).

[3]F. Pfeiffer, M. Bech, O. Bunk, P. Kraft, E. F. Eikenberry, C. Brönnimann, C. Grünzweig, and C. David, Nat. Mater. **7**, 134 (2008).

[4]M. Strobl, Sci. Rep. **4**, 7243 (2014).

[5]S. K. Lynch, V. Pai, J. Auxier, A. F. Stein, E. E. Bennett, C. K. Kemble, X. Xiao, W.-K. Lee, N. Y. Morgan, and H. H. Wen, Appl. Opt. **50**, 4310 (2011).

[6]W. Yashiro, Y. Terui, K. Kawabata, and A. Momose, Opt. Express **18**, 16890 (2010).

[7]P. Fratzl, H. F. Jakob, S. Rinnerthaler, P. Roschger, and K. Klaushofer, J. Appl. Crystallogr. **30**, 765 (1997).

[8]L. B. Gromann, F. De Marco, K. Willer, P. B. Noël, K. Scherer, B. Renger, B. Gleich, K. Achterhold, A. A. Fingerle, D. Muenzel, S. Auweter, K. Hellbach, M. Reiser, A. Baehr, M. Dmochewitz, T. J.

Schroeter, F. J. Koch, P. Meyer, D. Kunka, J. Mohr, A. Yaroshenko, H.-I. Maack, T. Pralow, H. van der Heijden, R. Proksa, T. Koehler, N. Wieberneit, K. Rindt, E. J. Rummeny, F. Pfeiffer, and J. Herzen, Sci. Rep. **7**, 4807 (2017).

[9]Z. Wang, N. Hauser, G. Singer, M. Trippel, R. A. Kubik-Huch, C. W. Schneider, and M. Stampanoni, Nat. Commun. **5**, 3797 (2014).

[10]H. Hetterich, N. Webber, M. Willner, J. Herzen, L. Birnbacher, S. Auweter, U. Schüller, F. Bamberg, S. Notohamiprodjo, H. Bartsch, J. Wolf, M. Marschner, F. Pfeiffer, M. Reiser, and T. Saam, Eur. J. Radiol. **94**, 38 (2017).

[11]M. Gresil, V. Revol, K. Kitsianos, G. Kanderakis, I. Koulalis, M. O. Sauer, H. Trétout, and A. M. Madrigal, Appl. Compos. Mater. **24**, 513 (2017).

[12]M. S. Nielsen, L. B. Christensen, and R. Feidenhans'l, Food Control **39**, 222 (2014).

[13]K. Creath, *V Phase-Measurement Interferometry Techniques* (Elsevier, 1988), pp. 349–393.

[14]H. Miao, L. Chen, E. E. Bennett, N. M. Adamo, A. A. Gomella, A. M. DeLuca, A. Patel, N. Y. Morgan, and H. Wen, Proc. Natl. Acad. Sci. **111**, 18799 (2014).

[15]C. Kottler, F. Pfeiffer, O. Bunk, C. Grünzweig, and C. David, Rev. Sci. Instrum. **78**, 043710 (2007).

[16]C. Arboleda, Z. Wang, and M. Stampanoni, Opt. Express **22**, 15447 (2014).

[17]M. Marschner, M. Willner, G. Potdevin, A. Fehringer, P. B. Noël, F. Pfeiffer, and J. Herzen, Sci. Rep. **6**, 23953 (2016).

[18]S. Bachche, M. Nonoguchi, K. Kato, M. Kageyama, T. Koike, M. Kuribayashi, and A. Momose, Sci. Rep. **7**, 6711 (2017).

[19]F. Bayer, S. Zabler, C. Brendel, G. Pelzer, J. Rieger, A. Ritter, T. Weber, T. Michel, and G. Anton, Opt. Express **21**, 19922 (2013).

[20]T. H. Jensen, M. Bech, O. Bunk, T. Donath, C. David, R. Feidenhans'l, and F. Pfeiffer, Phys. Med. Biol. **55**, 3317 (2010).

[21]V. Revol, C. Kottler, R. Kaufmann, A. Neels, and A. Dommann, J. Appl. Phys. **112**, 114903 (2012).

[22]F. Schaff, A. Malecki, G. Potdevin, E. Eggl, P. B. Noël, T. Baum, E. G. Garcia, J. S. Bauer, and F. Pfeiffer, Sci. Rep. **4**, 3695 (2014).

[23]G. Potdevin, A. Malecki, T. Biernath, M. Bech, T. H. Jensen, R. Feidenhans'l, I. Zanette, T. Weitkamp, J. Kenntner, J. Mohr, P. Roschger, M. Kerschnitzki, W. Wagermaier, K. Klaushofer, P. Fratzl, and F. Pfeiffer, Phys. Med. Biol. **57**, 3451 (2012).

[24]F. Prade, F. Schaff, S. Senck, P. Meyer, J. Mohr, J. Kastner, and F. Pfeiffer, NDT & E Int. **86**, 65 (2016).

[25]M. Kagias, Z. Wang, P. Villanueva-Perez, K. Jefimovs, and M. Stampanoni, Phys. Rev. Lett. **116**, 093902 (2016).

[26]M. Wieczorek, F. Schaff, F. Pfeiffer, and T. Lasser, Phys. Rev. Lett. **117**, 158101 (2016).

[27]Y. Sharma, F. Schaff, M. Wieczorek, F. Pfeiffer, and T. Lasser, Sci. Rep. **7**, 3195 (2017).